Triangularity Dependence of BOUT++ Nonlinear ELM Simulation Validation by DIII-D Fast Measurements

X. Q. Xu, T. Y. Xia, T. D. Rognlien, M. Umansky, I. Joseph, C. J. Lasnier, T. H. Osborne, L. Zeng

June 24, 2013

Disclaimer

This document was prepared as an account of work sponsored by an agency of the United States government. Neither the United States government nor Lawrence Livermore National Security, LLC, nor any of their employees makes any warranty, expressed or implied, or assumes any legal liability or responsibility for the accuracy, completeness, or usefulness of any information, apparatus, product, or process disclosed, or represents that its use would not infringe privately owned rights. Reference herein to any specific commercial product, process, or service by trade name, trademark, manufacturer, or otherwise does not necessarily constitute or imply its endorsement, recommendation, or favoring by the United States government or Lawrence Livermore National Security, LLC. The views and opinions of authors expressed herein do not necessarily state or reflect those of the United States government or Lawrence Livermore National Security, LLC, and shall not be used for advertising or product endorsement purposes.

Triangularity Dependence of BOUT++ Nonlinear ELM Simulation Validation by DIII-D Fast Measurements

M.E. Fenstermacher[1], X.Q. Xu[1], T.Y. Xia[1,2], T. D. Rognlien[1], M. Umansky[1], I. Joseph[1], C.J. Lasnier[1], T.H. Osborne[3] and L. Zeng[4]

[1]*Lawrence Livermore National Laboratory, Livermore, California 94550, USA*
[2]*Institute of Plasma Physics, Chinese Academy of Sciences, Hefei, China*
[3]*General Atomics, PO Box 85608, San Diego, California 92186-5608, USA*
[4]*University of California Los Angeles, Los Angeles, California 90095-7099, USA*

Abstract. Aspects of BOUT++ [1] nonlinear edge localized mode (ELM) simulations are compared with fast measurements from DIII-D ELMing H-mode plasmas for two different lower single-null (SN) plasma shapes. Simulations of small high frequency ELMs in a low triangularity (δ) SN shape, were performed with both three-field (magnetic flux $\tilde{A}_{\parallel}$, electric potential $\tilde{\Phi}$, and pressure $\tilde{p}$) [2] and six-field ($\tilde{n}_e$, $\tilde{n}_i$, $\tilde{T}_e$, $\tilde{T}_i$, $\tilde{A}_{\parallel}$, $\tilde{\Phi}$) [3] models in BOUT++, using the experimental X-point geometry and plasma collisionality. The 3-field non-linear ELM perturbation was coupled to the SOL model in the UEDGE fluid code [4] to calculate the evolution of the heat flux on the divertor target which compares well with the early evolution of the IR heat flux measurements. This extends the validation of BOUT++ ELM simulations beyond previous simulations [5] of large ELMs in a high-δ plasma.

Introduction and Motivation

Validated non-linear simulations of ELMs are needed to predict effects of ELM particle and energy bursts on plasma facing surfaces in future devices such as ITER, and to identify the level of ELM mitigation required of ELM control systems. ELM simulations with the BOUT++ code [1] are done at the low collisionality (v^*) characteristic of high power experiments and future large tokamaks, using a hyper-resistivity model [6] to avoid the unphysically large and vanishingly thin current layers typical of nonlinear MHD ELM simulations at low v^*. This model asserts that the electron viscosity is set by micro-turbulence and therefore comparable to turbulent electron thermal diffusivity. This allows the current sheets to diffuse at small scales, relaxes the ideal MHD constraint on magnetic field evolution and allows for ELM driven magnetic reconnection at finite current density.

Initial validation of three-field nonlinear simulations in high-δ DIII-D discharges with fast measurements [5] showed the importance of: (1) sufficient extent of the core grid to cover the ELM perturbation, (2) boundary conditions at the inner (core) side of the computational grid, (3) sufficient timescale to account for the total energy loss due to the ELM, and (4) extending to models with more field variables and sheath effects to simulate the density and temperature evolution separately in order to calculate target heat fluxes. Progress toward validation of three- and six-field simulations of low-δ ELMs against pedestal energy loss, pedestal density profile evolution through the ELM event, and fast target heat flux data is described below.

Experimental Results

The small Type-I ELM simulated for this work occurred in a low triangularity (δ=0.35) lower SN DIII-D H-mode discharge during a stationary phase with ELM frequency,
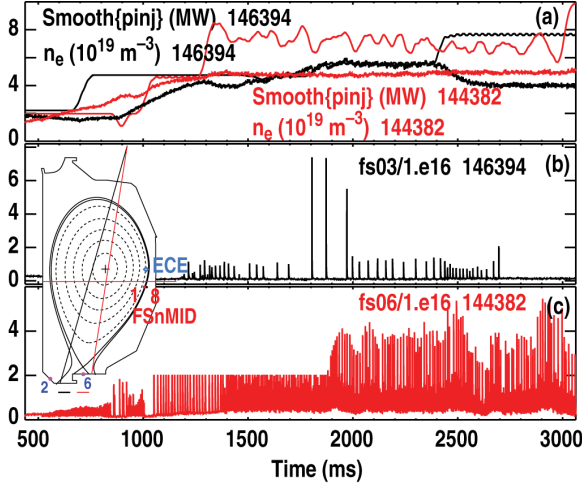
Fig. 1. Evolution of key parameters for DIII-D discharges 144382 (red) and 146394 (black) from which the ELMs at 2544.5 ms (red) and 2241 ms (black) were simulated with BOUT++, including (a) neutral beam power (MW) and line averaged density (10^{19} m^{-3}), and (b) plasma stored energy (MJ), and (c) outer divertor D_α emission (au). Insert shows equilibrium shape and diagnostic locations for signals in Fig. 2(a–f).
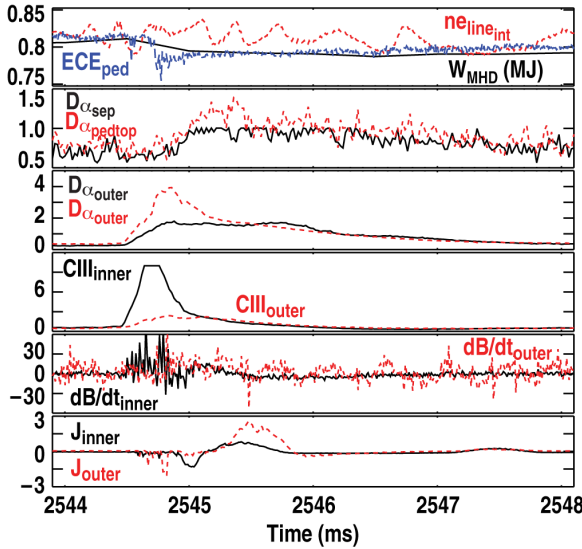

Fig. 2. Evolution of discharge 144382 ELM data including (a) total stored energy (MJ), line-integrated density along a horizontal midplane chord (10^{19} m^{-2}) and ECE emission near the top of the pedestal (au), (b) D_α emission from the top of the pedestal and near the separatrix at the LFS midplane (au), (c) D_α and (d) CIII (465 nm) emission from the ISP and LFS X-point (au), (e) dB/dt (T/s), and (f) ion saturation current [j_{sat} (au)] from the ISP and OSP.

$f_{\rm ELM}$~150 Hz, input power in feedback to hold constant normalized beta, $\beta_{\rm N} = 1.9$, and steady density (Fig. 1). Discharge parameters were $I_p = 1.16$ MA, $B_T = 2.15$ T, average $P_{\rm NBI} = 5.8$ MW, $R = 1.78$ m, $a = 0.58$ m, $\kappa = 1.72$, and $q_{95} = 4.0$. Comparing basic parameters with those from the high-δ, large ELM discharge used previously [5] shows similar n_e^{ped} and higher $P_{\rm NBI}$ (Fig. 1), but lower I_p and δ resulted in a factor of 2x lower T_e^{ped}, a factor of 4x higher ν^* and rapid smaller ELMs.

As in the larger ELM case [Fig. 2 of Ref. 5], the crash and recovery of the small ELM at 2544.5 ms (Fig. 2) were detected with multiple fast acquisition data chords in the pedestal, scrape-off layer (SOL) and divertor. Figure 2(a) shows that this ELM produced a drop in the plasma stored energy of 2% (17 kJ from a 0.8 MJ plasma). The most notable difference between this small ELM and the previous large ELM [5] is the slower evolution of the transient. The evolution on the outer midplane tangential D_α channels [Fig. 2(b)] is much slower than in the large ELM case, and the transients seen in the divertor [Fig. 2(c–f)] also evolve over a time about 2x longer. The inner vs. outer divertor asymmetric response is similar to the large ELM case with inner D_α response delayed compare to the outer divertor D_α [Fig. 2(c)], and the inner CIII response much larger than the outer CIII transient [Fig. 2(d)]. Similar to the large ELM case, the combined responses in Fig. 2(b–f) are consistent with both ion sound speed parallel

particle transport from an outer midplane ballooning instability [Fig. 2(b,c,f)] and effects of the detached inner leg burn-through by the ELM energy pulse [Fig. 2(d,e)], but here from a slower outer midplane perturbation. Fast density profiles from the outer midplane (Fig. 3) also showed a similar timescale for the drop of pedestal density and broadening into the SOL, followed first by recovery of the SOL and then pedestal build-up on longer timescales than for the large ELM [5]. Finally, fast target heat flux measurements (IRTV at 12 kHz) showed the ELM heat flux went predominantly to the outer strikepoint region (Fig. 4).

BOUT++ Simulations and Data Comparison

The ELM simulations in this paper were done with both three-field and six-field models. The three-field case ran through the non-linear ELM crash; to date, the six-field simulation has run into the initial non-linear growth phase. The simulations used the measured plasma profiles (n_e, T_e, T_i) in the pedestal (coherently averaged from the last 20% of the ELM cycle) and a kinetic EFIT consistent with those profiles. The radial electric field was calculated from force balance neglecting toroidal flow; comparison to the measured E_r showed similar pedestal well depth but a smaller inward width than the measured E_r well. The finite pressure in the SOL used for the kinetic EFIT was also used in BOUT++. As described in [5] non-ideal effects (e.g., finite resistivity, diamagnetic drift, etc.) are retained, the equations are solved for multiple modes using a field-aligned (flux) coordinate system, on a periodic domain in the parallel coordinate, and in toroidal angle, and a hyper-resistivity or electron viscosity term ($\nabla_\perp^4 A_\parallel$) is added to facilitate ELM magnetic reconnection with finite current sheets at the low ν^* in experiments ($\nu_e^* = 1.6$ and $\nu_i^* = 0.7$, for electrons and ions respectively).

The most extensive BOUT++ 6-field simulations were run with Dirichlet target plate BCs to over 2400 Alfvén times, giving 100 μs linear and >380 μs non-linear growth. They indicated that the plasma was unstable to peeling-ballooning modes with small linear growth rate, $\gamma/\omega_A = 0.03$. Comparison of the initial heat flux perturbation from the non-linear growth phase showed fine spatial structure similar to the outer target IR data. The long evolution of the linear + non-linear growth phases (~500 μs) is consistent with the measured slow buildup of this low δ ELM, in contrast to the rapid growth (~80 μs, both measurement and simulation) of the high δ, large ELM case [5].

The three-field simulations showed non-linear growth of the perturbation after 80 Alfvén times (~ 17 μs) of linear growth at $\gamma/\omega_A = 0.06$. Dirichlet (fixed pressure) boundary conditions (BCs) were used at the inner grid boundary ($\Psi_N = 0.8$) and Neumann (fixed gradient) BCs were used at the outer boundary. Figure 5 shows the 2D pressure perturbation 9 μs into the nonlinear phase.
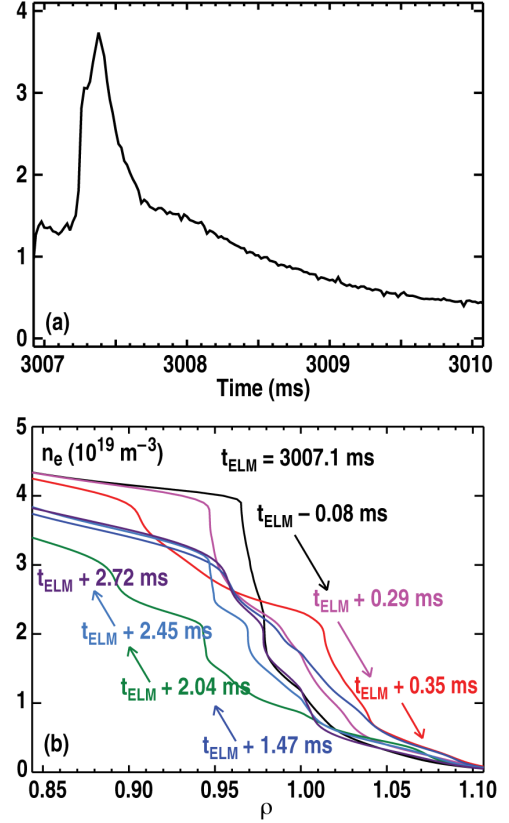
Fig. 3. Evolution of edge electron density profiles during the ELM with (a) temporal evolution from D_α emission in the outer divertor leg, and (b) multiple n_e profiles at times during the ELM evolution marked by vertical dashed lines in (a).
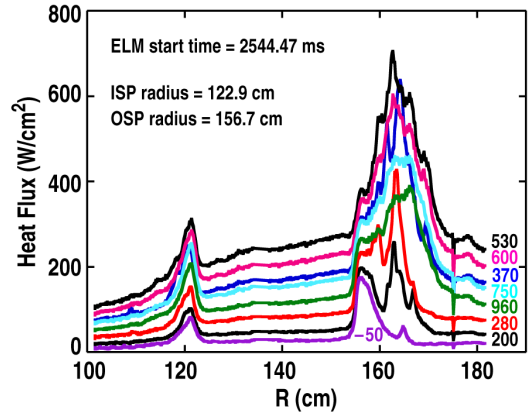
Fig. 4. Evolution of heat flux profile (W/cm²) vs. major radius (cm) on lower divertor target during ELM event. Times (μs) from ELM start time.
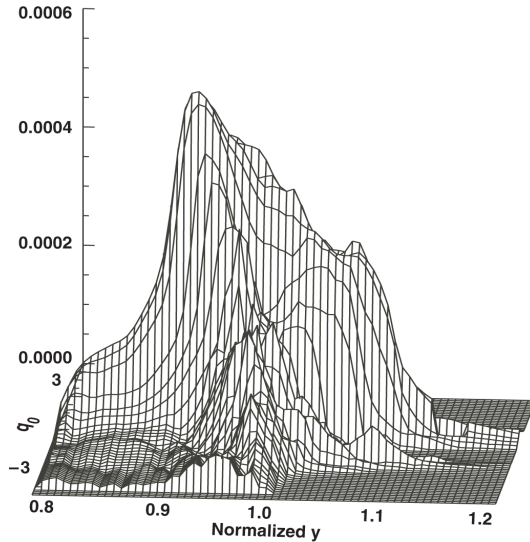
Fig. 5. 2D structure of the RMS pressure perturbation during the initial nonlinear ELM crash at t_{ELM} + 26 μs (poloidal angle (rad) referenced to outer midplane).
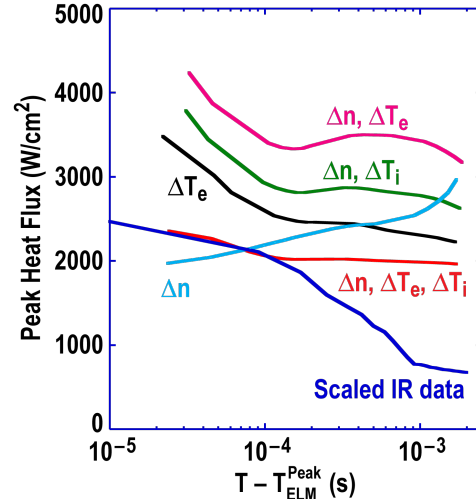

Fig. 6. Evolution of target peak heat flux for several distributions of BOUT++ pressure perturbation to density and temperature perturbations vs. IR data.

To estimate the target heat flux transient from these BOUT++ results, the pressure perturbation from Fig. 5 was used to generate an initial n_e, T_e, T_i perturbation for a time-dependent UEDGE calculation of the SOL/divertor plasma evolution. The perturbation was applied on the UEDGE grid to a solution well matched to the pre-ELM plasma with a fixed fraction carbon model. The best match to the initial target heat flux evolution timescale was obtained by assuming that the pressure perturbation was shared equally by n_e, T_e, and T_i (Fig. 6) consistent with coherent averaging of n_e and T_e data in the first 20% of the ELM cycle. The heat flux evolution using pure T_e or n_e perturbations (Fig. 6) was much faster or slower respectively than the IR data.

Summary

Results from a BOUT++ non-linear simulation of a small, 150 Hz ELM in a low δ LSN plasma were compared with fast ELM measurements and with results from a separate simulation of a large, 40 Hz ELM in a high δ plasma [5]. Using the BOUT++ ELM perturbation as input, a time-dependent UEDGE fluid model calculated a timescale of the heat flux transient relaxation comparable to measurements when the BOUT++ pressure transient was equally shared between n_e, T_e, and T_i. Initial six-field simulations of the ELM n_e, n_i, T_e and T_i perturbations are consistent with the longer non-linear evolution of this low-δ ELM.

[1] B.D. Dudson, *et al.*, Comp. Phys. Comm. **180**, 1467 (2009).

[2] X.Q. Xu, *et al.*, Phys. Rev. Lett. **105**, 175005 (2010).

[3] T.Y. Xia, X.Q. Xu and P.W. Xi, Nucl. Fusion **53**, 073009 (2013).

[4] T.D. Rognlien, J. Milovich, M. Rensink, G. Porter, J. Nucl. Mater. **196**, 347 (1992).

[5] M.E. Fenstermacher, X.Q. Xu, I. Joseph, M.J. Lanctot, C.J. Lasnier, *et al.*, J. Nucl. Mater. (2013) in press http://dx.doi.org/10.1016/j.jnucmat.2013.01.065

[6] X.Q. Xu, *et al.*, Nucl. Fusion **51**, 103040 (2011).